Title:

Experimental Investigation on a Rotating Detonation Cycle with Burned Gas Backflow

Author names and affiliations:

KEN MATSUOKA[a], MASAYA TANAKA[a], TOMOYUKI NODA[a], AKIRA KAWASAKI[a], JIRO KASAHARA[a]

[a] *Department of Aerospace Engineering, Nagoya University*
Furo-cho, Chikusa, Nagoya, Aichi 464-8603, Japan

Corresponding author:

KEN MATSUOKA
TEL: +81 29 853 3281
E-mail address: matsuoka@nuae.nagoya-u.ac.jp
Address: Furo-cho, Chikusa, Nagoya, Aichi 464-8603, Japan

Type of article:

Full-length article

Abstract

To analyze a rotating detonation cycle (RDC) with burned gas backflow, simultaneous self-luminous visualization, pressure, and thrust measurements with gaseous ethylene and oxygen were performed. Three different geometric blockage ratios (bottom-wall-surface area to cross-sectional area of combustor) were set at 89.2, 70.2, and 51.7%. The fuel and oxidizer mass flow rates and equivalence ratio were constant at 20.6 g/s, 41.2 g/s, and 1.7, respectively. During the combustion test, the single detonation wave rotated at 1557, 1459, and 1353 m/s, and the propagation speed increased proportionally for the geometric blockage ratio. The estimated fuel–oxidizer–based specific impulse was in the range of 148 ± 8 s, and the impact of the geometric blockage ratio and propagation speeds on this specific impulse was not confirmed. The hydrodynamic blockage ratio of the oxidizer injector due to the detonation wave was estimated using the oxidizer plenum pressure. It was found that the hydrodynamic blockage ratio linearly decreased with an increase in the geometric blockage ratio. This important trend suggests that the RDC operation is limited in the region of the lower geometric blockage ratio. It is also predicted that a reduction in the hydrodynamic blockage ratio while maintaining the geometric blockage ratio is required for stable RDC operation and achievement of pressure gain combustion. Moreover, the whole RDC structure including the burned gas back flow successfully visualized at the frame rate of 0.5 and 1 μs. The validity of estimated hydrodynamic blockage ratio was demonstrated by comparison with the visualization experiment. It was concluded that the hydrodynamic blockage ratio was primarily determined mainly by the time scale of the

burned gas backflow.

Keywords

Burned gas backflow, Injector, Pressure gain, Rotating detonation cycle, RDE

Nomenclature

a	=	oxidizer sound speed
A	=	cross-sectional area
BB	=	burned gas backflow
BR	=	blockage ratio
D_{CJ}	=	Chapman-Jouguet detonation speed
g	=	gravity acceleration
I_{sp}	=	specific impulse based on fuel and oxidizer
$\dot{m}$	=	mass flow rate
M	=	Mach number of the oxidizer
p	=	absolute pressure
R	=	oxidizer gas constant
t	=	time from ignition by explosive
T	=	oxidizer temperature

u_{fill} = filling velocity of mixture in z-axis direction

V_{det} = propagation speed of the rotating detonation wave

w = width of annular-shaped combustion chamber

z = central axis of combustor in which origin is at the bottom of the combustor

Greek symbols

γ = specific oxidizer heat ratio

Δt_{block} = duration for blocking the oxidizer injection slit

Δt_{cycle} = duration of one cycle of the rotating detonation wave

Subscripts

cal = calculation

CF = cold flow mode

DC = detonation combustion mode

eff = effective

exp = experiment

f = fuel

geo = geometric

hyd = hydrodynamic

ox = oxidizer

s = static

t = total

1. Introduction

As the heat release in a detonation wave originates behind a strong shock wave [1], the ideal thermal efficiency of a detonation cycle is higher than that of the Brayton cycle [2]. Furthermore, the detonation wave can propagate at approximately 2000 m/s and help reduce the combustor size. Thus, a detonative propulsion system has the potential to improve the specific impulse and thrust-to-weight ratio. To generate a detonation wave, a rotating detonation cycle (RDC) [3] in an annular combustor, a pulsed detonation cycle (PDC) [4] in a cylindrical combustor, and a reflective shuttling detonation cycle [5] in a plate-shaped combustor have been proposed. These methods repeat the (i) filling of fresh mixture, (ii) detonation propagation, and (iii) blowdown of high-pressure burned gas.

To realize a propulsion and power generation system driven by an RDC, studies are being conducted to validate the thrust performance and improve the understanding of the inner flow. For thrust measurement, Fotia et al. [6] performed a parametric study on the thrust performance of an air-breathing rotating detonation engine with gaseous hydrocarbon and hydrogen. Goto et al. [7] investigated the specific impulse and heat flux of a rotating detonation rocket engine with and without a throat under low ambient pressure conditions. Kawasaki et al. [8] showed the critical condition required by the inner radius to maintain a specific impulse. In a previous study related to

optical measurements, Rankin et al. [9] visualized chemiluminescence using an optically accessible outer body and reported a typical RDC structure. Chacon and Gamba [10] visualized chemiluminescence and shadowgraph images using a race-track shaped combustor. They reported the following three key non-ideal features: (i) a buffer region between the gases burned by the previous cycle and fresh mixture, (ii) parasitic combustion upstream of the detonation wave, and (iii) commensal combustion downstream of the detonation wave. Yokoo et al. [11] discussed the internal flow structures in a cylindrical RDC using a computed tomography technique.

All the above-mentioned studies focused on the combustor. However, it is important to discuss the burned gas backflow (BB) in an RDC because the high-pressure burned gas generated by a detonation wave strongly impacts the next detonation cycle. According to a theoretical analysis by Endo et al. [12], the burned gas pressure is approximately 7–10 times higher than the initial fresh mixture pressure when oxygen is used as an oxidizer. In general, a valveless injection method has been applied to the combustors. The high-pressure burned gas can propagate upstream of the combustor because the system has no mechanical blocker between the injector and combustor. Kubota et al. [13] and Matsuoka et al. [14] visualized and modeled the BB process using a semi-valveless PDC in which the cross-sectional area of the oxidizer inlet was the same as that of the combustor.

In contrast, in a typical RDC, the fuel and oxidizer are supplied into the combustor through a small hole or a narrow slit to prevent the BB. If the injection (plenum) pressure p_{-20} is sufficiently higher than the pressure p_0 at the bottom of the combustor, sonic injection is continuously maintained, and the detonation wave can stably propagate. In numerical approaches by Schwer et al. [15] and Fujii et al. [16], the BB process was not considered. However, a reduction in the total pressure loss via an injector with a large cross-sectional area is a critical issue to be considered to validate the detonation engine advantage. Bach et al. [17] experimentally demonstrated that the total burned gas pressure increased with an increase in the cross-sectional area of the oxidizer inlet. Paxson and Schwer [18] numerically clarified that the low total pressure loss (i.e., large cross-sectional area of air inlet) and the RDC stability were in a tradeoff relationship. The experiment by Bluemner et al. [19] suggested that the pressure feedback into the oxidizer plenum enhanced the lack of RDC stability. Thus, it is essential to understand the BB process in an RDC to achieve both high performance and stable operation. Using a planar laser-induced fluorescence (PLIF) method, Rankin et al. [20] investigated the blocked duration of an oxidizer injector by detonation wave. They reported that the hydrodynamic blockage ratio of the oxidizer injector by detonation wave was approximately 20% of the duration of one RDC cycle. However, the causal relationships between the BB process and the hydrodynamic/geometric blockage ratio has not been clarified.

In the present study, the RDC including the BB process was investigated by varying the geographic blockage ratio of the oxidizer slit. The steady-flow model was proposed for estimating the hydrodynamic blockage ratio of the oxidizer injector. The validity of the model was demonstrated by a visualization experiment where the RDC with the BB process was observed.

2. Experimental arrangement

2.1. Rotating detonation combustor for visualizing the burned gas backflow

Fig. 1 shows a cross-sectional view of the combustor used in the experiment. A polar coordinate system (z, r, θ) was set, with the bottom of the combustor as the origin. The center of the visualization window was defined as $\theta = 180°$ using the right-hand screw system.

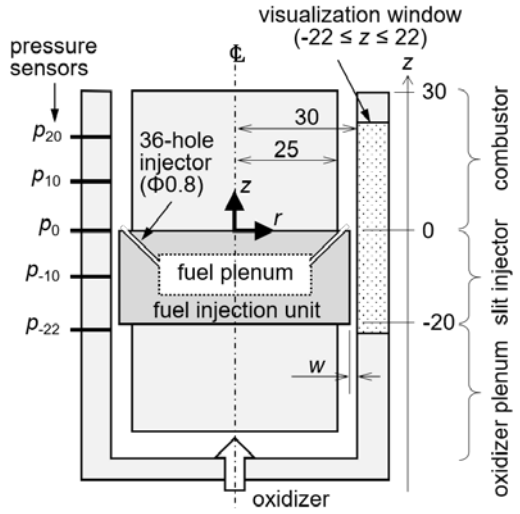

Fig. 1. Schematic cross-sectional view of rotating detonation combustor used in combustion test (unit: mm). Center of visualization area is defined as $\theta = 180°$. Pressure sensors (p_{20}, p_0, p_{-22}) and (p_{10}, p_{-10},) are respectively installed at (r, θ) = (30 mm, 67.5°) and (30 mm, 112.5°). The visualization area is $(z, r, \theta) = (-22\ \text{mm} \le z \le 22\ \text{mm}, r = 30\ \text{mm}, 162° \le \theta \le 198°)$.

Note that the subscript indicates the position along the z-axis. The dimensions of the annular-shaped combustion chamber were as follows: outer radius of 30 mm, inner radius of 25 mm, width of 5 mm, and length of 30 mm. A fuel injection unit (FIU) was installed in the area $-20\ \text{mm} \le z \le 0\ \text{mm}$. As shown in Fig. 1, fuel was injected into the combustor from a 36-hole injector with a diameter of 0.8 mm, and the injection direction was inclined at 45° with reference to the z-axis. Three different oxidizer slit widths, $w = 0.5, 1.4,$ and 2.3 mm were arranged by changing the outer diameter of the FIU. The geometric blockage ratio is defined by,

$$BR_{\text{geo}} = 1 - A_{-10}/A_{10}, \qquad (1)$$

where A_{-10} and A_{10} are the cross-sectional area of the oxidizer slit injector and the cross-sectional area of the combustor, respectively. Corresponding to each slit width w, the geometric blockage ratio was calculated as $BR_{\text{geo}} = 89.2, 70.2,$ and 51.7%. The total cross-sectional area of the fuel injector was $A_{\text{f}} = 18.1\ \text{mm}^2$, and the ratio of the cross-sectional area was $A_{\text{f}}/A_{-10} = 19.4, 7.0$ and 4.3% for $w = 0.5, 1.4,$ and 2.3 mm, respectively. If air is used as an oxidizer, the area ratio is calculated at $A_{\text{f}}/A_{-10} = 3.9, 1.4,$ and 0.9% under the assumption that the mass flow rate of fuel, equivalence ratio, and total pressure at the oxidizer plenum were the same as the experimental conditions and the oxidizer was choked at the injector exit.

To observe the BB process, the visualization window was set in the area of $(z, r, \theta) = (-22\ \text{mm} \le z \le 22\ \text{mm}, r = 30\ \text{mm}, 162° \le \theta \le 198°)$. Five 5 kHz pressure sensors (Keller, PAA-23)

were installed at $z = 20, 10, 0, -10,$ and -22 mm and pressures p_{20}, p_{10}, p_0, p_{-10}, and p_{-22} were measured. The experimental frequency of the RDC was 8.4 ± 0.6 kHz and higher than that of the pressure sensor. In the present study, the time-averaged static pressure instead of the dynamic pressure of the detonation wave was required. The pressure validity has been demonstrated as a capillary tube averaged pressure [21, 22] The combustor was fixed on a slide-type thrust stand, and the thrust was measured by a load cell (Aikoh Engineering, DUD-200K), having a system error of 4 N obtained by the previous calibration test.

2.2. Experimental conditions

Corresponding to the three geometric blockage ratios of $BR_{\mathrm{geo}} = 89.2, 70.2,$ and 51.7%, the experiment numbers were named as BR90, BR70, and BR50, respectively. Gaseous ethylene and oxygen were used as the fuel and oxidizer, respectively. The injection pressure of the fuel was constant at 0.62 ± 0.2 MPa. BR_{geo} was changed while maintaining the mass flow rate of the fuel and oxidizer by the choking orifice set in each feed line upstream of the combustor. From the previous calibration test, the mass flow rate and equivalence ratio in the combustion test were estimated at $\dot{m}_{\mathrm{f}} = 20.6 \pm 0.4$ g/s, $\dot{m}_{\mathrm{ox}} = 41.2 \pm 0.5$ g/s, and $ER = 1.7 \pm 0.1$. The thrust stand was set in a 30 m^3 chamber, and the back pressure was in the range $p_{\mathrm{b}} = 13 \pm 6$ kPa before and after the combustion test. The room temperature was constant at $T_{\mathrm{t}} = 285 \pm 2$ K.

Self-luminosity in the combustor was observed both along both the *z*-axis and the direction normal to the *z*-axis. The wave number and propagation speed of the detonation wave were confirmed by a high-speed camera (Vision Research, Phantom V 2011) with a 12-bit gradation set in the *z*-axis direction. The frame speed and exposure time were set at 430 kfps (2.3 μs/frame) and 900 ns, respectively. The RDC structure with the BB process was observed using a high-speed camera (Shimadzu, HPV-X2) with a 10-bit gradation set normal to the *z*-axis, and no band-pass filter was used. The frame speed and exposure time were 2 Mfps (0.5 μs/frame) and 200 ns for BR90 and BR70, respectively, and 1 Mfps (1.0 μs/frame) and 500 ns for BR50. The sampling rate of the pressure sensors and load cell was 1 MHz.

3. Results and discussion

3.1. Time history of pressure, thrust, and time-averaged propagation speed

Fig. 2 shows the time history of each pressure and load cell output observed in BR90. At $t = -600$ ms, the input signal of the valve supplying the oxidizer switched ON, and each pressure increased proportionally to the gas supply. At $t = 0$ ms, the ignition signal was applied to the explosive igniter. The combustion mode started at approximately $t = 7$ ms and rapidly shifted to the steady-state combustion mode. The regions of $-1 \text{ ms} \leq t \leq 0 \text{ ms}$ and $100 \text{ ms} \leq t \leq 101 \text{ ms}$ were defined as the cold flow (CF) and detonation combustion (DC) modes, respectively.

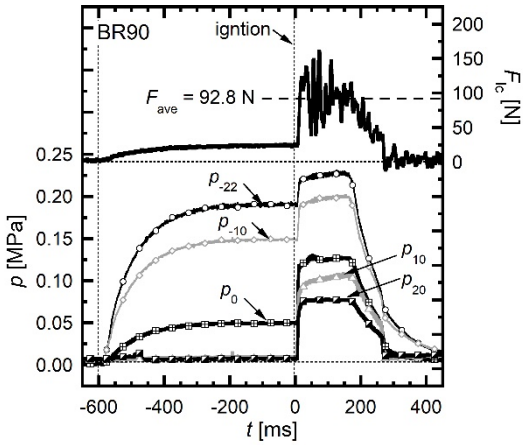

Fig. 2. Time history of load cell output (top) and static pressures (bottom) measured at $z = -22, -10, 0, 10,$ and 20 mm under the condition of geographic blockage ratio $BR_{\mathrm{geo}} = 89.2\%$.

Fig. 3 shows the time-averaged pressure along the *z*-axis during the CF and DC modes. At $\mathrm{z} \geq 10$ mm, the tendencies of the pressure gradients during CF and DC were similar in BR90, BR70, and BR50. This result indicates that the burned gas acceleration process was approximately the same despite the different BR_{geo}. In contrast, a large pressure gradient was observed $\mathrm{z} \leq -10$ mm in BR90, and the oxidizer flow in the plenum was stagnated. It is interesting to note that the pressure ratio $p_{-22,\mathrm{DC}}/p_{-22,\mathrm{CF}}$ increased with a decrease in BR_{geo}. The amount of BB increased as the effective injection area decreased. Consequently, the plenum pressure must have increased to maintain the mass flow rate $\dot{m}_{\mathrm{ox}}$. Thus, the pressure increase probably indicates the amount of blocked injection area (i.e., hydrodynamic blockage ratio) due to the BB process. In contrast, the fuel injection was not affected by detonation propagation because the fuel plenum pressure of 0.62 ± 0.2 MPa was sufficiently higher than the combustion pressure during the DC mode.

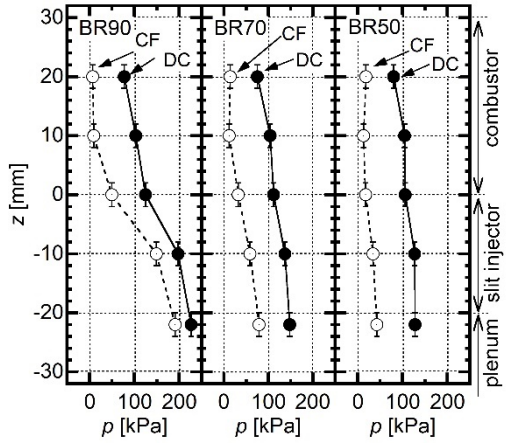

Fig. 3. Time-averaged pressures during detonation combustion (DC) and cold flow (CF) modes.

As shown in Fig. 2, the time-averaged thrust in the duration of $50\ \text{ms} \leq t \leq 150\ \text{ms}$ was $F_{\text{ave}} = 92.8, 85.0, \text{and } 91.5\ \text{N}$ in BR90, BR70, and BR50, respectively. The fuel–oxidizer-based specific impulse was evaluated using Eq. (2).

$$I_{\text{sp}} = \frac{F_{\text{ave}}}{(\dot{m}_{\text{ox}} + \dot{m}_{\text{f}})g}, \qquad (2)$$

where $g = 9.81\ m/\text{s}^2$ is the gravity acceleration. The specific impulse was calculated at $I_{\text{sp}} = 153 \pm 7, 140 \pm 7, \text{and } 151 \pm 7\ \text{s}$ for BR90, BR70, and BR50, respectively, and the standard deviation of the mean of the mass flow rate and the load cell system error were taken into account for the propagation error. This result indicates that the impact of BR_{geo} on the specific impulse was not confirmed.

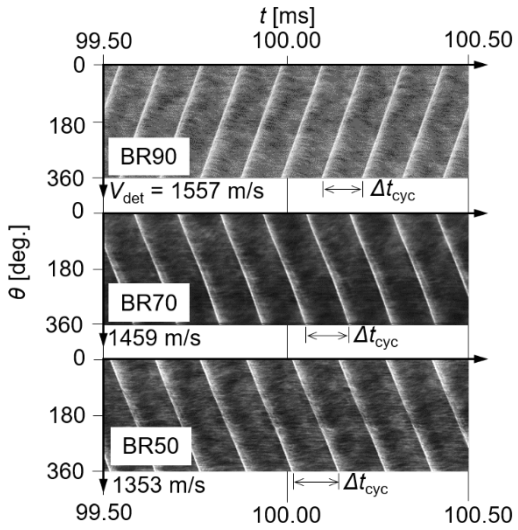

Fig. 4. $t-\theta$ diagram of chemiluminescence taken along z-axis. Radius was constant at 27.5 mm (center radius of combustor).

Fig. 4 shows a $t-\theta$ diagram of the central combustor radius $r = 27.5\,\mathrm{mm}$, based on the visualization along the *z*-axis. As the single detonation wave propagated, the rotation direction of θ was negative for BR90 and positive for BR70 and BR50. The 10-cycle averaged propagation speed was $V_{\mathrm{det}} = 2\pi r/\Delta t_{\mathrm{cycle}} = 1557 \pm 3, 1459 \pm 3, \mathrm{and}\ 1353 \pm 3\ \mathrm{m/s}$. These values were 60, 55, and 51% of D_{CJ} [23], calculated using $p_{0,\mathrm{DC}}$ (experimental pressure at the combustor bottom in DC mode), *ER*, and T_t. The deficit in the propagation speed was caused by various phenomena that occurred due to the decrease in BR_{geo}. For example, transverse waves play an essential role in detonation propagation. Radulescu and Lee [24] investigated the impact of transverse waves using a porous-wall tube. They experimentally confirmed that the detonation became weaker or collapsed in the porous wall region. In the present study, the main fresh mixture was produced near the outer

combustor wall. When BR_{geo} decreased, the transverse wave disappeared in the bottom-wall-less situation. In addition, the lack of fuel and oxidizer mixing [25] and deflagration combustion upstream and downstream of the detonation front [10] were also considered.

3.2. Injection pressure and effective oxidizer injection area

In this section, the hydrodynamic blockage ratio BR_{hyd} of the oxidizer injection area during the DC mode is discussed. BR_{hyd} is defined by Eq. (3).

$$BR_{\mathrm{hyd}} = \left[1 - \frac{(A_{\mathrm{eff}})_{\mathrm{DC}}}{(A_{\mathrm{eff}})_{\mathrm{CF}}}\right]_{\mathrm{z=0}}, \qquad (3)$$

where A_{eff} is the effective oxidizer injection area in each mode. When the BB occurred, $A_{\mathrm{eff,DC}}$ became smaller than $A_{\mathrm{eff,CF}}$ and, BR_{hyd} changed in response to the amount of backflow. Eq. (3) can be arranged in Eq. (4) by assuming that (i) the flow of each mode was a steady flow, (ii) the mass flow rate of the oxidizer $\dot{m}_{\mathrm{ox}}$, gas constant of the oxidizer R, and total temperature of the oxidizer T_{t} were constant regardless of the mode.

$$BR_{\mathrm{hyd}} = \left[1 - \frac{\left[p_{\mathrm{t}}\sqrt{\gamma\left(\frac{2}{\gamma+1}\right)^{\frac{\gamma+1}{\gamma-1}}}\right]_{\mathrm{CF}}}{\left[p_{\mathrm{t}}\sqrt{\frac{2\gamma}{\gamma-1}\left\{\left(\frac{p_{\mathrm{s}}}{p_{\mathrm{t}}}\right)^{\frac{2}{\gamma}} - \left(\frac{p_{\mathrm{s}}}{p_{\mathrm{t}}}\right)^{\frac{\gamma+1}{\gamma}}\right\}}\right]_{\mathrm{DC}}}\right]_{\mathrm{z=0}}, \qquad (4)$$

where p_{t}, p_{s}, and γ are the total pressure, static pressure, and ratio of the oxidizer specific heat, respectively. In Eq. (4), choked and unchoked flows were assumed in the CF and DC modes, respectively.

The isentropic relationships at $z = -22$ mm are expressed by Eqs. (5) and (6):

$$\left(\frac{p_\mathrm{t}}{p_\mathrm{s}}\right)_{z=-22} = \left[\left(1 + \frac{\gamma - 1}{2}M^2\right)^{\frac{\gamma}{\gamma-1}}\right]_{z=-22}, \qquad (5)$$

$$\left(\frac{T_\mathrm{t}}{T_\mathrm{s}}\right)_{z=-22} = \left[1 + \frac{\gamma - 1}{2}M^2\right]_{z=-22}, \qquad (6)$$

where T_s is the static oxidizer pressure. The mass flow rate $\dot{m}_\mathrm{ox}$ and sound speed a of the oxidizer at $z = -22$ mm were obtained from Eqs. (7) and (8), respectively:

$$\dot{m}_\mathrm{ox} = (\rho u A)_{z=-22}, \qquad (7)$$

$$a = \left(\sqrt{\gamma R T_\mathrm{s}}\right)_{z=-22}, \qquad (8)$$

where ρ and u are the density and flow velocity of the oxidizer at $z = -22$ mm, respectively. By substituting Eqs. (6), (7), and (8) and the stated equation of ideal gas ($p = \rho RT$) in the formula for the Mach number ($M = u/a$), the following equation was eventually obtained.

$$\left[M^2\left(1 + \frac{\gamma - 1}{2}M^2\right)\right]_{z=-22} = \left[\left(\frac{\dot{m}_\mathrm{ox}}{p_\mathrm{s}A}\right)^2 \frac{RT_\mathrm{t}}{\gamma}\right]_{z=-22}, \qquad (9)$$

The Mach number M_{-22} was estimated using Eq. (9). The total pressure $p_{-22,\mathrm{t}}$ was calculated using Eq. (5), $p_\mathrm{s} = p_{-22}$, and M_{-22}. Assuming an isentropic flow between the oxidizer plenum and the injector exit, BR_hyd was obtained by Eq. (4), $p_\mathrm{s} = p_0$, and $p_{0,\mathrm{t}} = p_{-22,\mathrm{t}}$. In the actual calculation, the following values were used: $\dot{m}_\mathrm{ox} = 41.2 \pm 0.5$ g/s, $A_{-22} = 864$ mm^2, $R = 260$ J kg^{-1}K^{-1}, $\gamma = 1.40$, and $T_\mathrm{t} = 285 \pm 2$ K. A steady flow was assumed in this model. As shown in Fig. 4, the deviation of the propagation speed V_det was less than 1% under all conditions. This result suggests that the macroscopic characteristics, such as the time-averaged static pressure p_s, mass flow rate ($\dot{m}_\mathrm{f}, \dot{m}_\mathrm{ox}$),

and hydrodynamic blockage ratio BR_{hyd} were constant even though the microscopic detonation mechanism was unsteadily changed.

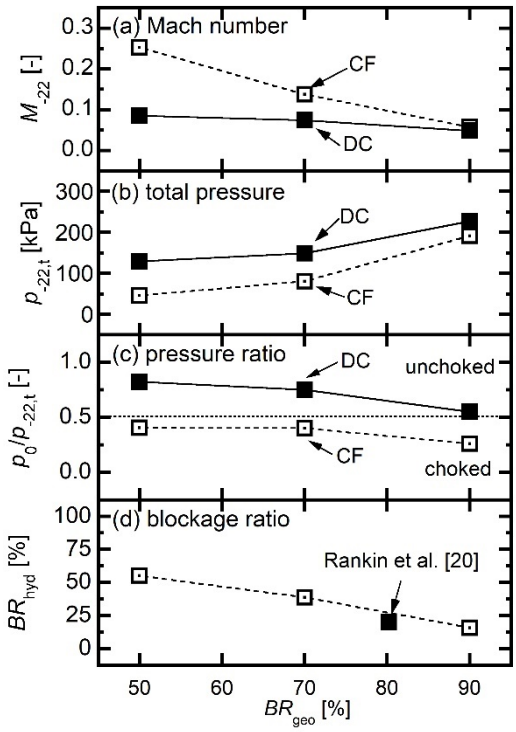

Fig. 5. (a) Mach number at oxidizer plenum (z = -22 mm), (b) total pressure at oxidizer plenum (z = -22 mm), (c) pressure ratio of measured pressure at injector exit (z = 0 mm) on total pressure, and (d) effective blockage ratio of oxidizer injector during detonation combustion mode. DC: detonation combustion mode, CF: cold flow mode.

Figs. 5(a) and (b) show M_{-22} and $p_{-22,\mathrm{t}}$, respectively. In the CF mode (open symbols in Fig. 5), M_{-22} linearly decreased with BR_{geo}. This shift in the inner flow resulted in an increase in the total pressure loss [26] between the choked orifice, and $z = -22$ mm as shown in Fig. 5(b). In other words, the specific impulse of BR50 was approximately equal to that of BR90 and BR70, despite the same total pressure (injection pressure). Fig. 5(c) shows the ratio of the experimental pressure

$p_{0,s} = p_0$ to the estimated total pressure $p_{-22,t}$ in the plenum. As mentioned above, it was assumed that $p_{-22,t}$ was equal to $p_{0,t}$ at the injector exit. The horizontal dashed line in Fig. 5 (c) shows the critical pressure ratio of $p_0/p_{-22,t} = p_0/p_{0,t} = 0.53$ ($\because \gamma = 1.40$). This result indicates that the oxidizer was injected into the combustor in the choked/unchoked conditions for the CF/DC modes, respectively.

By substituting $p_{-22,t}$ and p_0 for p_t and p_s in Eq. (4), the hydrodynamic blockage ratio BR_{hyd} was determined. As shown in Fig. 5(d), BR_{hyd} linearly decreased with an increase in BR_{geo}. If the effective injection area $A_{eff,CF}$ in the CF mode was equal to the geometric injection area A_{-10}, the effective injection area $A_{eff,DC}$ in the DC mode could be obtained by $A_{eff,DC} = (1 - BR_{hyd})A_{-10}$. The actual injection area in the DC mode was estimated at $A_{eff,DC} = 78.8, 157.8,$ and 186.3 mm^2 for BR90, BR70, and BR50, respectively. The actual oxidizer injection area was maximized for the lowest value of BR_{geo}. The closed symbol in Fig. 5(d) shows the result of the visualization experiment by Rankin et al. [20] and is approximately consistent with the proposed model. This important trend suggests that the RDC operation is limited in the region of a lower geometric blockage ratio. It is also predicted that a reduction in the hydrodynamic blockage ratio while maintaining the geometric blockage ratio is required for stable RDC operation and achieving pressure gain combustion. In the next section, the validity of BR_{hyd} is verified with the help of a visualization experiment.

3.3. Flow field of rotating detonation cycle with burned gas backflow

Fig. 6 shows the distribution of the self-luminous intensity in the $\theta - z$ and $t - z$ diagram.

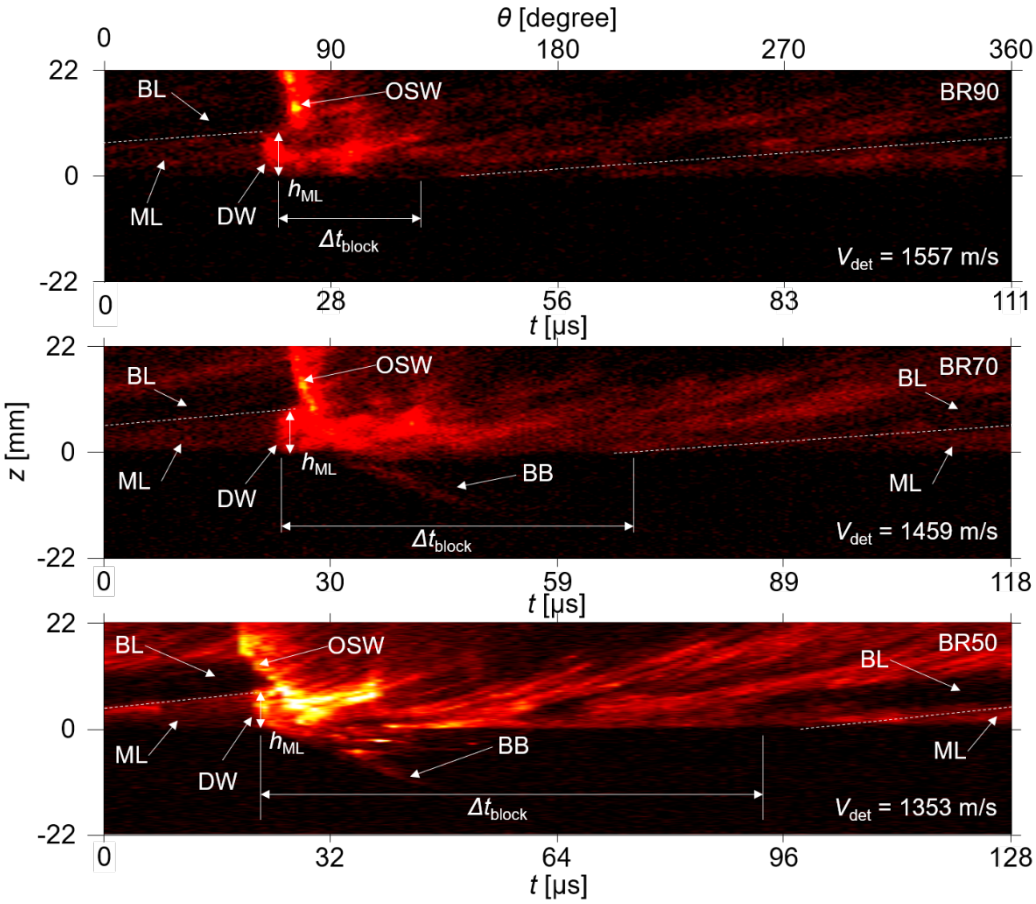

Fig. 6. Distribution of self-luminous intensity in $\theta - z$ and $t - z$ diagram, θ axis was transformed by the duration $\Delta t_{\mathrm{cycle}}$ required for one RDC. BB: backflow of burned gas, BL: buffer layer, DW: detonation wave, ML: mixture layer, OSW: oblique shock wave. See video image.

Note that the propagation direction of the detonation wave was set in the negative direction of θ under all conditions. This $\theta - z$ diagram was constructed using the following two processes: (i) The center-line pixels of the visualization window $(z, \theta) = (-22\ \mathrm{mm} \leq z \leq 22\ \mathrm{mm}, \theta = 180°)$ were integrated in the time direction and the $t - z$ diagram was constructed, and (ii) the t-axis of the $t - z$ diagram was transformed to the θ-axis by the duration $\Delta t_{\mathrm{cycle}}$ required for one RDC. Note that

the corresponding duration $\Delta t_{\mathrm{cycle}}$ in Fig. 6 was different for each of the conditions because the propagation speed V_{det} of the detonation wave was different, the high-intensity region did not indicate the chemiluminescence intensity, and a qualitative analysis was not possible because of the different exposure times.

The low- and middle-intensity regions were confirmed in front of the high-intensity region. The former and latter were probably fuel-rich buffer layer (BL) and mixture layer (ML), respectively. The fuel injection pressure was sufficiently higher than that of the oxidizer, and the cross-sectional area of the fuel injector hole was considerably smaller than that of the oxidizer. Thus, the BB impact on the fuel injection was small, and fuel injection was started at the beginning of the mixture-refilling process. This fuel-rich BL has been confirmed by Chacon and Gamba [10]. The ML probably consisted of fuel, oxidizer, and burned gas. Thus, low self-luminous intensity was probably the non-ideal parasitic combustion also suggested by Chacon and Gamba [10].

In the high-intensity region, a detonation wave (DW) propagating in ML and the following oblique shock wave (OSW) were observed. The DW shape was different under each condition. Because the mixing degree in ML was spatially non-uniform due to multi-hole fuel injection, the DW propagated while changing the shape (see video movie). Recently, the three-dimensional propagation behavior of DW has been investigated using a numerical approach [27]. Visualization techniques can be used to observe the shock wave and mixture filling process in the combustor with a small BR_{geo}. These

are important for understanding the three-dimensional mechanism of RDCs.

It was confirmed that the OSW angle was unlike the ideal case where the rotating detonation propagated in a spatially uniform premixed mixture [28]. According to the numerical calculations by Fujii et al. [16] and Sato et al. [27], it was predicted that the OSW angle increased in the case of a non-premixed and/or non-uniform mixture. In the region behind the DW, BB in the negative z-axis direction was confirmed, especially in BR70 and BR50. The BB was triggered by the high-pressure burned gas generated by the DW. The BB probably occurred in BR90, but it could not be confirmed due to the narrow-slit width w of the oxidizer injector. After the BB, the refilling process of the fuel and oxidizer was initiated at different times. Finally, BL and ML were produced.

In Fig. 6, the duration $\Delta t_{\mathrm{block}}$ for blocking the oxidizer slit is shown. $\Delta t_{\mathrm{block}}$ was estimated at $\Delta t_{\mathrm{block}} = BR_{\mathrm{hyd}} \times \Delta t_{\mathrm{cycle}} = 17.4, 46.0, \text{and } 70.7\ \mu s$ for BR90, BR70, and BR50, respectively. The trajectory of the contact surface between ML and BL is also shown, denoted by the dashed line and extrapolated to the negative θ-axis direction. $\Delta t_{\mathrm{block}}$ can roughly predict the leading tip where the ML refilling process begins. This result implies that the increase in the ratio of the oxidizer plenum pressure in the RDC operation was determined by the blocked injector due to the BB.

As shown in Fig. 6, the detonation height h_{ML} was measured at $h_{\mathrm{ML}} = 10.2$, 9.7, and 8.4 mm for BR90, BR70, and BR50, respectively. If the filling velocity u_{fill} of the mixture was constant, the velocity was evaluated at $u_{\mathrm{fill,exp}} = h_{\mathrm{ML}}/\left(\Delta t_{\mathrm{cycle}} - \Delta t_{\mathrm{block}}\right) = 109,\ 135 \text{ and } 147$ m/s. From the

momentum conservation of the jet before and after the fuel and oxidizer impinging, the mixing filling velocity after impinging was calculated at $u_{\mathrm{fill,cal}} = 292, 237, \text{and } 213\ \mathrm{m/s}$. The difference was primarily due to the abrupt expansion at the oxidizer inlet exit. The experimental velocity $u_{\mathrm{fill,exp}}$ most likely becomes closer to $u_{\mathrm{fill,cal}}$ when BR_{geo} approaches zero.

4. Conclusion

Self-luminous visualization, pressure, and thrust measurements were simultaneously performed to investigate an ethylene–oxygen RDC with BB. While maintaining the mass flow rate of the fuel and oxidizer, three different geometric blockage ratios (bottom-wall-surface area/cross-sectional area of combustor) were set at $BR_{\mathrm{geo}} = 89.2, 70.2, \text{and } 51.7\%$ (BR90, BR70, and BR50). As a result of the combustion test, the following three conclusions were drawn.

(1) The single detonation wave propagated at a constant speed of $V_{\mathrm{det}} = 1557 \pm 10, 1459 \pm 10, \text{and } 1353 \pm 10\ \mathrm{m/s}$ in BR90, BR70, and BR50. The propagation speed increased in proportion to the increase in BR_{geo}. The time-averaged thrust was $F_{\mathrm{ave}} = 92.8, 85.0, \text{and } 91.5\ \mathrm{N}$. The fuel-oxidizer-based specific impulses were estimated at $I_{\mathrm{sp}} = 153 \pm 10, 140 \pm 10, \text{and } 151 \pm 10\ \mathrm{s}$. In this study, the impact of BR_{geo} on the specific impulses were not confirmed.

(2) The Mach number and the total pressure in the oxidizer plenum were estimated using an isentropic flow. The Mach number (total pressure) decreased (increased) with an increase in BR_{geo}. Moreover, it was suggested that the oxidizer was injected as a choked flow in the CF mode and as an

unchoked flow in the DC mode. The actual oxidizer injector blockage ratio (hydrodynamic blockage ratio BR_{hyd}) was predicted using measured time-averaged pressures and a steady-flow assumption. As a result, it was found that BR_{hyd} linearly decreased with an increase in BR_{geo}. This important trend suggests that the RDC operation is limited in the region of the lower geometric blockage ratio. It is also predicted that a reduction in the hydrodynamic blockage ratio while maintaining the geometric blockage ratio is required for stable RDC operation and achievement of pressure gain combustion. The universality of this trend should be validated because the relationship between BR_{hyd} and BR_{geo} is probably dominated by the mixing method, geometry, composition of mixture, etc.

(3) A whole RDC structure including the burned gas backflow successfully visualized at the frame rate of 0.5 and 1 μs. A fuel-rich buffer layer (BL) and a non-ideal mixture layer (ML) were observed in front of the detonation wave. The high-intensity region consisted of the detonation wave and the following oblique shock wave. It was observed that BB started behind the detonation wave. The hydrodynamic blockage ratio BR_{hyd}, which is estimated using a steady-flow model and an increase in the ratio of the oxidizer plenum pressure in detonation combustion mode, can predict the leading tip where the ML refilling process begins. This result implies that the increase in the ratio of the oxidizer plenum pressure in RDC operation was determined by the blocked injector due to the BB.

Acknowledgements

This work was supported by a Grand-in-Aid for Scientific Research (A) (No. 17H04971).

References

[1] J. H. S. Lee, The Detonation Phenomena, NY, USA, 2008.

[2] W.H. Heiser, D.T. Pratt, Thermodynamic Cycle Analysis of Pulse Detonation Engines, J. Propul. Power 18 (2002) 68−76.

[3] F. A. Bykovskii, S. A. Zhdan, E. F. Vedernikov, Continuous Spin Detonations, J. Propul. Power 22 (2006) 1204−1216.

[4] K. Kailasanath, Recent Developments in the Research on Pulse Detonation Engines, AIAA J. 41 (2003) 145−159.

[5] M. Yamaguchi, T. Taguchi, K. Matsuoka, A. Kawasaki, J. Kasahara, H. Watanabe, A. Matsuo, Investigation of combustion modes and pressure of reflective shuttling detonation combustor, Proc. Combust., Accepted for publication, July 21, 2020.

[6] M. L. Fotia, J. L. Hoke, F. R. Schauer, Experimental Performance Scaling of Rotating Detonation Engines Operated on Gaseous Fuels, J. Propul. Power 33 (2017) 1−10.

[7] K. Goto, J. Nishimura, A. Kawasaki, K. Matsuoka, J. Kasahara, A. Matsuo, I. Funaki, D. Nakata, M. Uchiumi, K. Higashino, Propulsive Performance and Heating Environment of Rotating Detonation Engine with Various Throat Geometries, J. Propul. Power 35 (2019) 213−223.

[8] A. Kawasaki, T. Inakawa, J. Kasahara, K. Goto, K. Matsuoka, A. Matsuo, I. Funaki, Critical Condition of Inner Cylinder Radius for Sustaining Rotating Detonation Waves in Rotating Detonation Engine Thruster, Proc. Combust. 37 (2019) 3461−3469.

[9] B. A. Rankin, D. R. Richardson, A. W. Caswell, A. G. Naples, J. L. Hoke, F. R. Schauer, Chemiluminescence Imaging of an Optically Accessible Non-Premixed Rotating Detonation Engine, Combust. Flame 176 (2017) 12−22.

[10] F. Chacon and M. Gamba, Study of Parasitic Combustion in an Optically Accessible Continuous Wave Rotating Detonation Engine, AIAA SciTech Forum (2019), AIAA 2019-0473.

[11] R. Yokoo, K. Goto, A. Kawasaki, K. Matsuoka, J. Kasahara, A. Matsuo, I. Funaki, Experimental Study of Internal Flow Structures in Cylindrical Rotating Detonation Engines, Proc. Combust., Accepted for publication, August 3, 2020

[12] T. Endo, J. Kasahara, A. Matsuo, K. Inaba, S. Sato, T. Fujiwara, Pressure History at the Thrust Wall of a Simplified Pulse Detonation Engine, AIAA J. 42 (2004) 1921−1930.

[13] A. Kubota, K. Matsuoka, A. Kawasaki, J. Kasahara, A. Matsuo, H. Watanabe, T. Endo, Optical Measurement of Fluid Motion in Semi-Valveless Pulse Detonation Combustor with High-Frequency Operation, Combust. Sci. Technol. 192 (2018) 197−212.

[14] K. Matsuoka, H. Taki, A. Kawasaki, J. Kasahara, H. Watanabe, A. Matsuo, T. Endo, Semi-

Valveless Pulse Detonation Cycle at a Kilohertz-scale Operating Frequency, Combust. Flame 205 (2019) 434−440.

[15] D. Schwer, K. Kailasanath, Numerical Investigation of the Physics of Rotating-Detonation-Engines, Proc. Combust. 33 (2011) 2195−2202.

[16] J Fujii, Y. Kumazawa, A. Matsuo, S. Nakagami, K. Matsuoka, J. Kasahara, Numerical Investigation on Detonation Velocity in Rotating Detonation Engine Chamber, Proc. Combust. 36 (2017) 2665−2672.

[17] E. Bach, P. Stathopoulos, C. O. Paschereit, M. D. Bohona, Performance analysis of a rotating detonation combustor based on stagnation pressure measurements, Combust. Flame 217 (2020) 21−36.

[18] D. E. Paxson, D. A. Schwer, Operational Stability Limits in Rotating Detonation Engine Numerical Simulations, AIAA SciTech Forum (2019), AIAA 2019-0748.

[19] R. Bluemner, M. D. Bohon, C. O. Paschereit, E. J. Gutmark, Effect of inlet and outlet boundary conditions on rotating detonation combustion, Combust. Flame 216 (2020) 300−315.

[20] B. A. Rankin, C. A. Fugger, D. R. Richardson, K. Y. Cho, J. Hoke, A. W. Caswell, J. R. Gordand, F. Schauer, Evaluation of Mixing Processes in a Non-Premixed Rotating Detonation Engine Using Acetone PLIF, 54th AIAA Aerospace Sciences Meeting (2016), AIAA 2016-1198.

[21] C. A. Stevens, M. Fotia, J. Hoke, F. Schauer, Comparison of Transient Response of Pressure Measurement Techniques with Application to Detonation Waves, 53rd AIAA Aerospace Sciences Meeting (2015) AIAA 2015-1102.

[22] R. Yokoo, K. Goto, J. Kim, A. Kawasaki, K. Matsuoka, J. Kasahara, A. Matsuo, I. Funaki, Propulsion Performance of Cylindrical Rotating Detonation Engine, AIAA J., Published Online 20 Nov. 2019.

[23] S. Gordon, B. J. McBride, NASA Reference Publication 1311 (1996), https://www.grc.nasa.gov/WWW/CEAWeb/

[24] R. Radulescu, J. H. S. Lee, The Failure Mechanism of Gaseous Detonations Experiments in Porous Wall Tubes, Combust. Flame 131 (2002) 29−46.

[25] J. Burr, K. H. Yu, Mixing in Linear Detonation Channel with Discrete Injectors and Side Relief, AIAA SciTech Forum (2019) AIAA 2019-1014.

[26] K. Matsuoka, M. Esumi, K. B. Ikeguchi, J. Kasahara, A. Matsuo, I. Funaki, Optical and Thrust Measurement of a Pulse Detonation Combustor with a Coaxial Rotary Valve, Combust. Flame 159 (2012) 1321−1338.

[27] T. Sato, V. Raman, Detonation Structure in Ethylene/Air-Based Non-Premixed Rotating Detonation Engine, J. Propul. Power, Published Online 27 May 2020.

[28] R. T. Fievisohn and K. H. Yu, Steady-State Analysis of Rotating Detonation Engine Flowfields with the Method of Characteristics, J. Propul. Power 33 (2017) 89−99.

Figure and video captions

Fig. 1. Schematic cross-sectional view of rotating detonation combustor used in combustion test (unit: mm). Center of visualization area is defined as $\theta = 180°$. Pressure sensors (p_{20}, p_0, p_{-22}) and (p_{10}, p_{-10},) are respectively installed at (r, θ) = (30 mm, 67.5°) and (30 mm, 112.5°). Visualization area is $(z, r, \theta) = (-22\ \text{mm} \le z \le 22\ \text{mm}, r = 30\ \text{mm}, 162° \le \theta \le 198°)$.

Fig. 2. Time history of load cell output (top) and static pressures (bottom) measured at $z = -22, -10, 0, 10,$ and 20 mm under the condition of geographic blockage ratio $BR_{\text{geo}} = 89.2\%$.

Fig. 3. Time-averaged pressures during detonation combustion (DC) and cold flow (CF) modes.

Fig. 4. $t - \theta$ diagram of chemiluminescence taken along z-axis. Radius was constant at 27.5 mm (center radius of combustor).

Fig. 5. (a) Mach number at oxidizer plenum (z = -22 mm), (b) total pressure at oxidizer plenum (z = -22 mm), (c) pressure ratio of measured pressure at injector exit (z = 0 mm) on total pressure, and (d) effective blockage ratio of oxidizer injector during detonation combustion mode. DC: detonation combustion mode, CF: cold flow mode.

Fig. 6. Fig. 6. Distribution of self-luminous intensity in $\theta - z$ and $t - z$ diagram, θ axis was transformed by duration Δt_{cycle} required for one RDC. BB: backflow of burned gas, BL: buffer layer, DW: detonation wave, ML: mixture layer, OSW: oblique shock wave. See video image.

Video Moving images observed by a high-speed camera set normal to the z-axis. Playing/recording speeds are 15 fps/2 Mfps for BR90 and BR70, and 7.5 fps/1 Mfps for BR50.